

Computerized segmentation and diagnostics of whole-body bone scintigrams

Luka Šajn¹, Igor Kononenko¹, Metka Milčinski²

¹University of Ljubljana
Faculty of Computer and Information Science
Tržaška 25, SI-1001 Ljubljana, Slovenia
{luka.sajn, igor.kononenko}@fri.uni-lj.si

²University Medical Centre
Department for Nuclear Medicine
Zaloška 7, SI-1525 Ljubljana, Slovenia
metka.milcinski@kclj.si

8th January 2007

Author responsible for correspondence: Luka Šajn¹, phone +386 41 795 980

Abstract

Bone scintigraphy or whole-body bone scan is one of the most common diagnostic procedures in nuclear medicine. Since expert physicians evaluate images manually some automated procedure for pathology detection is desired. A robust knowledge based methodology for segmenting body scans into the main skeletal regions is presented. The algorithm is simultaneously applied on anterior and posterior whole-body bone scintigrams. Expert knowledge is represented as a set of parameterized rules, used to support standard image processing algorithms. The segmented bone regions are parameterized with algorithms for classifying patterns so the pathologies can be classified with machine learning algorithms. This approach enables automatic scintigraphy evaluation of pathological changes, thus in addition to detection of point-like high-uptake lesions also other types can be discovered.

Our study includes 467 consecutive, non-selected scintigrams. Automatic analysis of whole-body bone scans using our segmentation algorithm gives more accurate and reliable results than previous studies. Preliminary experiments show that our expert system based on machine learning closely mimics the results of expert physicians.

Keywords: whole-body bone scan, automatic segmentation, image processing, machine learning

1 Introduction

Whole-body scan or whole body bone scintigraphy is a well known clinical routine investigation and one of the most frequent diagnostic procedures in nuclear medicine [1]. Indications for bone scintigraphy include benign and malignant diseases, infections, degenerative changes and other clinical entities [2]. Bone scintigraphy has high sensitivity and the changes of the bone metabolism are seen earlier than the changes in bone structure detected on skeletal radiograms [1].

The investigator's role is to evaluate the image, which is of technically poor resolution due to the physical limitations of gamma camera. There are approximately 158 bones visible on anterior and posterior whole-body scans [3]. Poor image resolution and the number of bones to recognize make the evaluation of images difficult. Some research on automating the process of counting the bone lesions has been done but only a few studies attempted to automatically segment individual bones prior to the computerized evaluation of bone scans [4; 5; 6].

1.1 Related work

First attempts to automate scintigraphy in diagnostics for thyroid structure and function were made in 1973 [7]. Most of the research on automatic localization of bones has been performed at the former Institute of medical information science at the University of Hildesheim in Germany from 1994 to 1996. The main contribution was made by Bernauer [4] and Berning [5] who developed semantic representation of the skeleton and evaluation of the images. Benneke [6] has realized their ideas in 1996.

Yin and Chiu [8] tried to find lesions using a fuzzy system. Their pre-processing of scintigrams includes rough segmentation of six fixed-size regions, regardless of individual image properties. Those parts are rigid and not specific enough to localize a specific bone. Their approach for locating abnormalities in bone scintigraphy is limited to point-like lesions with high uptake.

When dealing with lesion detection, other authors like Noguchi [3] have been using intensity thresholding and manual lesion counting or manual bone region of interest (ROI) labelling. Those procedures are only sufficient for more evident pathologies whereas new emerging pathological regions could be overlooked.

2 Aim and our approach

The aim of our study is to develop a robust algorithm for segmenting whole-body bone scans. Some possible methods for individual bone extraction are also presented. Segmented scans allow further development of automated procedures for recognition of pathological condition in specific bone regions.

When a scintigraphy is observed by an expert physician, each bone region is diagnosed according to several possible pathologies (lesions, malignom, metas-

tasis, degenerative changes, inflammation, other pathologies or no pathologies). The process of detecting the lesions can be aided by some advanced machine learning classifier [9] which produces independent diagnoses. The implementation of such system was also the aim of the study. It can be used as a tool to remind a physician of some possibly overlooked spots or even to give some additional insight in the problem. It also enables further studies of individual bone regions with other algorithms (e.g. pattern classification or custom tailored algorithms).

In order to achieve a robust segmentation algorithm we have defined the most characteristic bone regions and the most identifiable points in those regions (reference points, Figure 1). Those points are chosen so that they can be uniformly identified over all distinct images in as many cases as possible, which is necessary since the images and skeletons vary considerably (Figure 2).

There are some algorithms for detecting image features (e.g. Scale Invariant Feature Transform - SIFT [10]). Since the scintigrams are so variable, one cannot rely solely on features detected in images alone, but has to use some existing background knowledge. In our case this background knowledge is human anatomy.

Because scintigrams are represented by relatively small images, many algorithms (e.g. PCA [11], image correlation) are not appropriate or directly applicable. The idea is to use simple and easy to control algorithms. In our study we have used several image processing algorithms such as binarization, dilatation, skeletonization, Hough's transform, Gaussian filtering [12], beam search, circle fitting and ellipse fitting with least square method (LSM), in combination with background knowledge of anatomy and scintigraphic patterns.

The experience with segmentation and pathology classification is presented. The steps of segmentation and diagnosing are shown on Figure 3.

3 Materials and methods

3.1 Patients and images

Retrospective review of 467 consecutive, non-selected scintigraphic images from 461 different patients investigated at Nuclear medicine department, University Medical Centre in Ljubljana, from October 2003 to June 2004 was performed. Images were not preselected, so the study included representative distribution of patients committed to examination in 9 months. Images contained some artifacts and non-osseous uptake such as urine contamination and medical accessories (i.e. urinary catheters) [13]. In addition, site of radiopharmaceutical injection is frequently visible (obstructs the image).

21% of the images were diagnosed as normal with no artifacts, meaning that no pathologies and no artifacts were present. 60% of the images were diagnosed with slight pathology regardless to artifacts, 18% with strong pathology and 1%

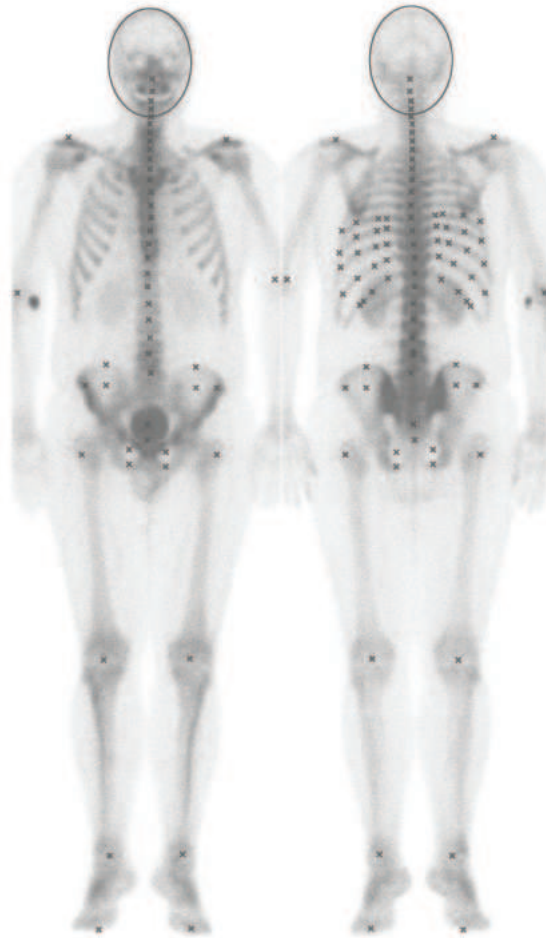


Figure 1: Defined characteristic reference points

of the images was classified as super-scans. Super-scan is obtained when the patient has very strong pathologies, which absorb most of the radiopharmaceutical so the other bone regions are vaguely visible.

In 18% of the images, partial scans (missing a part of the head or upper/lower extremities in the picture) were acquired, which complicates the segmentation process. There were also children/adolescents with growth zones (5% of the images), manifested as increased osteoblastic activity in well delineated areas with very high tracer uptake.

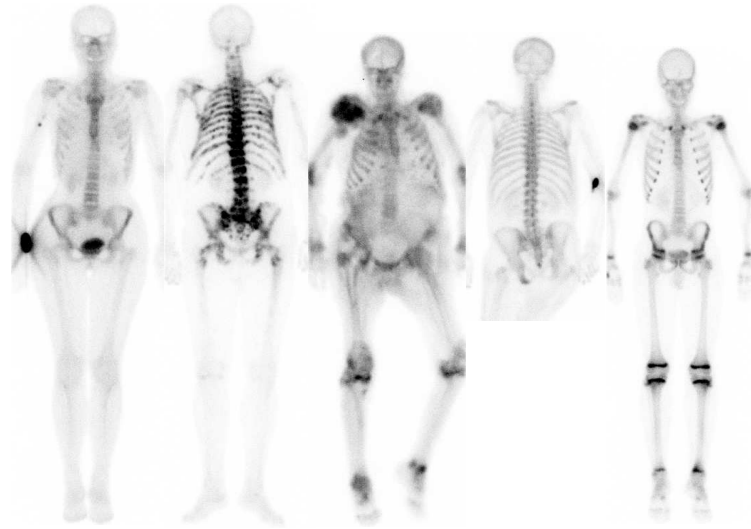


Figure 2: Examples of scintigrams and skeletal variety

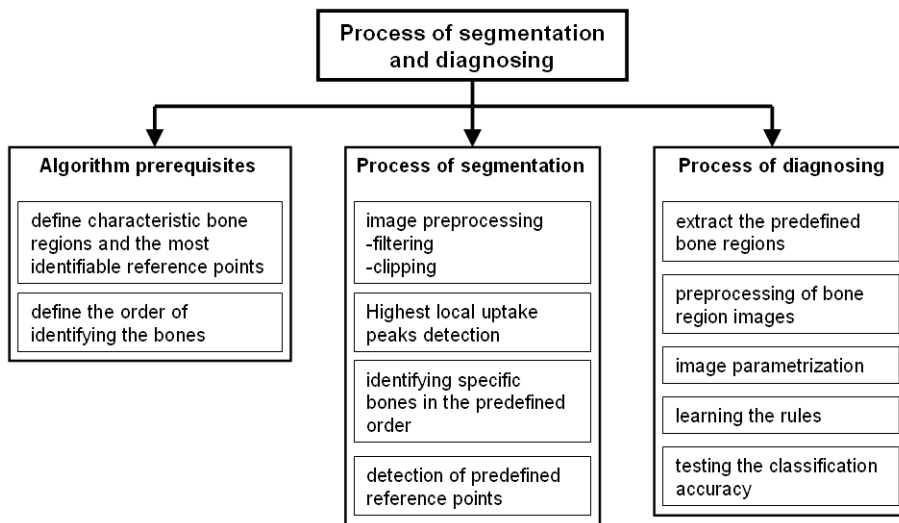


Figure 3: Algorithm steps

3.2 Bone scintigraphy

All patients were scanned with gamma camera model Siemens MultiSPECT with two detectors, equipped with LEHR (Low Energy High resolution) colli-

mators. Scan speed was 8cm per minute with no pixel zooming. Technetium labelled phosphonate (99m-Tc-DPD, Technos^R) was used. Bone scintigraphy was obtained 2-3 hours after intravenous injection of 750 MBq of radiopharmaceutical. The whole body field was used to record anterior and posterior views digitally with resolution 1024 x 256 pixels (approx. 205cm x 61cm). Images represent counts of detected gamma decays in each spatial unit with 16-bit grayscale depth.

3.3 Detection of reference points

Bone scans vary considerably in their size, contrast, brightness and skeletal structure (Figure 2). In practice many scans are only partial because only a determined part of the body is observed or due to the scanning limitations when the patient is too obese to fit in the screening area.

The idea of detecting the reference points is to find an image region which can easily be found in most cases. This region's reference point is then used as a starting location for the further reference point detection. Further reference point search is guided with the background knowledge of the spatial relations between bone regions and specific bones. Following image processing algorithms aid the search within some predefined boundaries (regions of interest - ROIs): beam search, dynamic binarization, dilatation, skeletonization, circles and ellipses fitting using LSM. Afterwards all detected reference points are shifted vertically and horizontally to the neighboring regions with the highest uptake (intensity).

In our study we have observed that on only two images out of 467 the shoulders were not visible. Many other possible starting points could have been missing on the images more often (i.e. head, arms, one or both legs). Therefore shoulders have been chosen as the main bone region to start with. Second and the last assumption is the upward orientation of the image. This assumption is not limiting since all scintigraphies are made with the same upward orientation.

In order to make the detection of reference points faster (linear complexity) and more reliable we have tried to automatically detect peaks which would roughly cover the reference points and build some structural skeleton for reference point search guidance. The idea is similar to the SIFT ([10]) algorithm, where image features are also represented by the most outstanding pixels over different resolutions.

3.3.1 Detection of the reference points candidates (peaks)

There are numerous methods for detecting image peaks. We have tried several. SIFT [10] method returned too few peaks to guarantee a robust region detection on vast variety of skeletons. Another more classic image filters like Canny edge detection returned too many peaks. Peaks with such filters can be acquired by connecting the peaks to polylines, which are then reduced to vertices. We have tried another custom tailored approach, which is based on orthogonal two-way Gaussian and linear filtering and mimics the SIFT algorithm. The algorithm

smooths the image with the averaging window, which size was experimentally determined. The algorithm 1 works as shown in the pseudo-code.

Algorithm 1 Detect relevant peaks Ω

Require: original image $I[x_i, y_j], i \in [0, m - 1], j \in [0, n - 1]$; Gaussian filter

$$G_{3 \times 3} = \left(\frac{1}{16} \begin{bmatrix} 1 & 2 & 1 \\ 2 & 4 & 2 \\ 1 & 2 & 1 \end{bmatrix} \right); \text{ size of averaging window } W (w \times h \text{ where } w \text{ and } h \text{ are odd});$$

d - minimal distance between detected peaks;

$$W_{w \times h} = \left(\frac{2}{w+h} \begin{bmatrix} 1 & 2 & \dots & \frac{w+1}{2} & \dots & 2 & 1 \\ 2 & 3 & \dots & \frac{w+1}{2} + 1 & \dots & 3 & 2 \\ \vdots & \vdots & & \vdots & & \vdots & \vdots \\ \frac{h+1}{2} & \frac{h+1}{2} + 1 & \dots & \frac{w+h}{2} & \dots & \frac{h+1}{2} + 1 & \frac{h+1}{2} \\ \vdots & \vdots & & \vdots & & \vdots & \vdots \\ 2 & 3 & \dots & \frac{w+1}{2} + 1 & \dots & 3 & 2 \\ 1 & 2 & \dots & \frac{w+1}{2} & \dots & 2 & 1 \end{bmatrix} \right)$$

Ensure: relevant set of peaks Ω

- 1: $I_1 \leftarrow I \times G$ {Gaussian filter applied}
 - 2: $I_2 \leftarrow I_1 \times W_{w \times h}$ {bigger linear averaging filter applied}
 - 3: add all elements from I_2 to Ω_1 where both left and right hand-side elements in I_2 have lower intensities {horizontal pass}
 - 4: add all elements from I_2 to Ω_1 where both upper and lower elements in I_2 have lower intensities {vertical pass}
 - 5: sort Ω_1 by element intensities
 - 6: add consecutively all elements from Ω_1 to Ω where minimal distance of element to $\Omega > d$
-

The limited level of radioactivity injected due to radiation protection regulation in typical studies causes low intensities (count levels of gamma rays) which causes vague images of bone scans. Bone edges are better visible after images are filtered with some averaging algorithm (i.e. wavelet based, median or Gaussian filter) [12]. A Gaussian filter is used in order to enhance the detection of peaks. The image is smoothed with the Gaussian filter where the pixels of higher intensities (> 90 gamma rays per pixel) are set to the predefined upper limit (90). Images smoothed in such a way are less prone to be obstructed by high intensity lesions or artifacts since at this stage we are interested only in finding anatomical reference points and not possible lesions.

In the case of scintigraphic images we may introduce scale variant methods since the nature of this image modality guaranties a fixed scale (100 pixels $\approx 24cm$). The size of the averaging window $W_{w \times h}$ was experimentally set to 11×5 ($\approx 2.6cm \times 1.2cm$) as it gave best results by the means of segmentation accuracy.

The reference points 1 are searched for using the detected peaks (Figure 4). Both images, anterior and posterior, are simultaneously processed in the

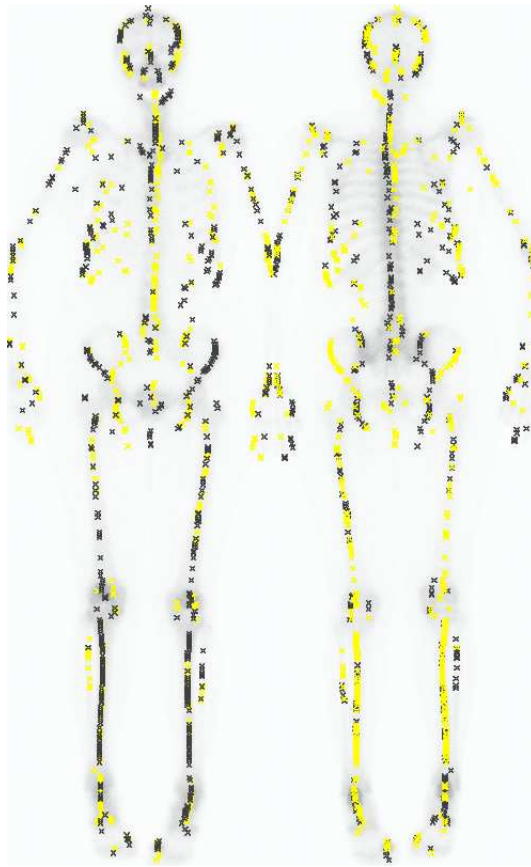


Figure 4: Example of detected image peaks on anterior and posterior image using the algorithm 1 ($d = 1, w \times h = 11 \times 5$) (all peaks are mirrored to the counter image)

same detection order. Detected points from the anterior image are mirrored to the posterior and vice versa. Mirroring is possible since both images are taken at the same time and are therefore aligned and have the same size. Some point $pt_{(x,y)}$ on one image is mirrored to the other one as $pt'_{(x',y')}$ where $x' = image_width - x, y' = y$ on the other image. Some bones are better visible on the anterior and some on the posterior images due to the varying distances from the collimators (gamma-ray sensors). In each step the detected reference points visible in both images are compared. The algorithm chooses the one, which is estimated to better represent the desired reference point. For each reference point type (knee, ankle, ilium, pubis, shoulders ...) we have determined the

rules which decide better choice.

When deciding the better reference point of the anterior and posterior scan two aspects are observed. The expected neighboring uptake and relations to other detected reference points on the basis of expected skeletal ratios (e.g. the length of the upper arm - humerus is expected to be approximately $0.67 * \text{length of the spine}$ - spanning from the neck nape to the sacrum bone). More detailed algorithms (source code) can be found in [14].

Bigger bone regions have the same shape and position in both images but usually the edge of one side of the bone is better expressed on one image due to the distance to collimator whereas the other side is better expressed on the other image. With combining peaks from both anterior and posterior images both sides are clearly expressed (i.e. ilium bone). Some bone regions (i.e. skull, ilium, pubic bones etc.) can be represented by some basic geometric shapes (i.e. circles, lines and ellipses) which can be determined by using the LSM method. The fitting of the geometric shapes is improved also using the mirrored points from anterior to posterior image and vice versa.

The order, in which the reference points were detected, was determined using the knowledge of the human anatomy as well as physicians' recommendations. The anatomical knowledge is represented as a list of parameterized rules specific to each bone region. Rule parameters (e.g. thresholds, spatial and intensity ratios, etc.) were initially set by physicians and further refined on a separate tuning set.

Respective skeletal regions are processed in the following order: shoulders, pelvis, head, thorax and extremities.

3.3.2 Shoulders.

The two shoulder reference points as the main starting points are detected with the first peaks (4) found from diagonal directions (Figure 5). ROIs dimensions are estimated to be (190pixels, 40cm) high and wide 30% of the image width. ROIs starting point is in the left and right upper image corner. Relative ratios for ROI size regarding the image width were estimated experimentally.

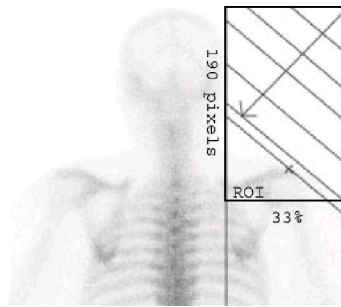


Figure 5: Locating shoulders

The next step is to locally shift the candidate points within their ROIs (14×7 pixels) to the region with highest uptake. Only in 5 images out of 467, shoulders were not found correctly due to the tilted head position which obstructed the diagonal direction detection.

From both detected reference shoulder points already some information can be attained. The shoulder width (distance between left and right shoulder reference point) and the inclination (angle between left and right shoulder) can be calculated. The detected shoulder reference points, their distance (shoulder width) and inclination are used for calculating the expected relative sizes of other bone regions and their respective orientations (i.e. estimated spine length is determined as $shoulder_{width} \times 1.76$). This way other lengths are estimated as well and are also used to estimate the respective ROI sizes which are used to localize the search of other reference points.

3.3.3 Pelvic region (ilium bone, pubis bone, great trochanter of femur).

The pelvis is located at the end of the spine and has approximately the same width as the shoulders. In order to find the pelvis, the estimation of the spine position is required. This is performed with a beam search (Figure 6(a)). The beam is represented with a rectangle with a certain length and width. One end of the beam is determined as the middle point of the line between the shoulders and it's orientation is perpendicular to the shoulder line. The angle at which the beam covers most peaks is a rough estimation of spine direction since there is most of the uptake in the vertebrae and hence peaks are dense in that region. With the use of calculated peaks we speed up the process because there is no need for calculating the cumulative uptake within each beam. It suffices to count the peaks covered by the beam. The most identifiable bone in pelvic region is the ilium bone which has higher uptake values than it's neighboring soft tissue. The ilium bone has a circular shape in the upper part and is therefore convenient for circle fitting with LSM. This bone is well described with already detected peaks as shown in Figure 6(b). The ilium position is roughly estimated with ROIs which are found on the basis of the skeleton's anticipated ratios and reference points found up to this step of detection (details can be obtained at [14]).

The pubis bone is detected by estimating the pubis ROI using the detected ilium location, distance between detected ilium circle centers and the angle between them. The experimentally determined ROI's size is narrowed with the binarization algorithm. Pixels are binarized with some threshold which produces a certain ratio between black and white pixels. ROI is narrowed so that 60% of the ROI is covered with black (binarized) pixels. Additional vertical peaks are calculated inside the estimated ROI using the algorithm 1 with smaller averaging window $W_{w \times h}$ (7×3 pixels). Circles representing the two ilium and pubic bones are detected with LSM using the detected peaks as shown in Figure 6(b). Circle localization is improved with 3 runs in which the LSM is run first

and then the peaks with greater distance to the detected circle ($> 12 \times r$) are removed and the procedure starts again. With this procedure more descriptive circles bounding the circular-shape bones are acquired.

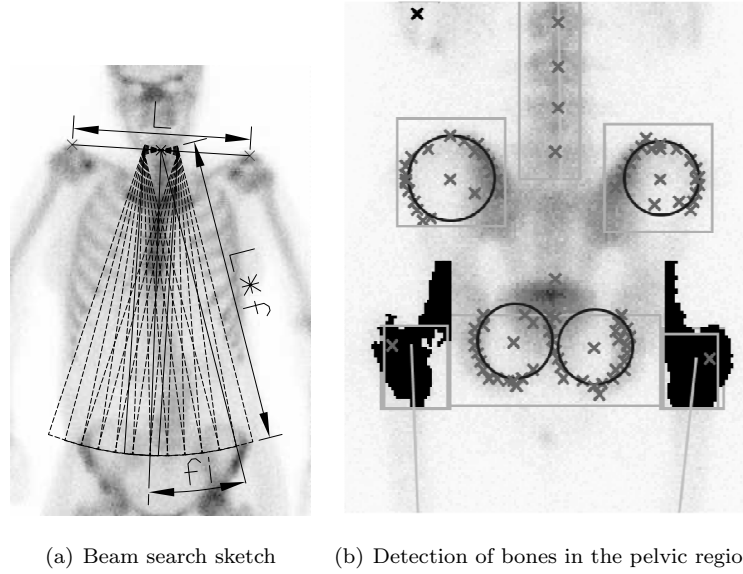


Figure 6: Beam search and detection in pelvic region

3.3.4 Head and neck.

When at least the image orientation and the location of the shoulders are known, some part of the neck or the head is visible between the shoulders. Finding the head is not difficult but its orientation is, especially in cases where a part of the head is not visible in the scan. The most reliable method for determining head orientation and position is ellipse fitting of the head contour. The head contour is determined with the horizontal scan from both left and right side to the first pixel exceeding the predefined threshold. The thresholding is used to find the head edge above the shoulders as shown in Figure 7(a) where the contour is depicted with small points.

The head contour is further processed with the LSM algorithm for fitting the ellipse which best describes the head position and its orientation.

The general quadratic equation for an ellipse in xy -plane is a second order polynomial

$$a_{11}x^2 + 2a_{12}xy + a_{22}y^2 + b_1x + b_2y + c = 0 \quad (1)$$

All conic sections are represented by this equation. The ellipses are those for which $a_{11}a_{22} - a_{12}^2 > 0$. It can be shown [15] that using this restriction the

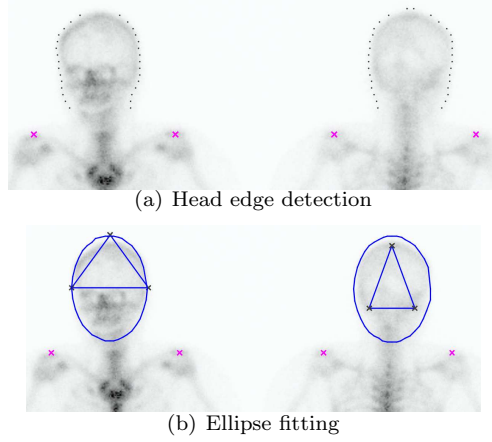


Figure 7: Head detection

center of an ellipse $C(k_1, k_2)$ is given by the following equation

$$C(k_1, k_2) = \frac{(a_{22}b_1 - a_{12}b_2, a_{11}b_2 - a_{12}b_1)}{2(a_{12}^2 - a_{11}a_{22})}. \quad (2)$$

The main axes and orientation can be expressed with polynomial coefficients.

Let $\mu = 1/(a_{11}k_1^2 + 2a_{12}k_1k_2 + a_{22}k_2^2 - c)$ and define $m_{11} = \mu a_{11}$, $m_{12} = \mu a_{12}$, and $m_{22} = \mu a_{22}$. Set $\lambda_1 = ((m_{11} + m_{22}) + \sqrt{(m_{11} - m_{22})^2 + 4m_{12}^2})/2$. The semiminor axis b of the ellipse is $b = \frac{1}{\sqrt{\lambda_1}}$. The semimajor axis is calculated in similar way. Set $\lambda_2 = ((m_{11} + m_{22}) - \sqrt{(m_{11} - m_{22})^2 + 4m_{12}^2})/2$. The semimajor axis a is $a = \frac{1}{\sqrt{\lambda_2}}$.

The angle formed by the major axis with the positive x -axis Θ satisfies the equation $\tan(2\Theta) = -\frac{a_{12}}{a_{22} - a_{11}}$.

Equation 1 can be solved using the LSM and from obtained coefficients all ellipse parameters representing head can be expressed. The experiments showed very good results regarding head orientation and hence detection of the neck (Figure 8).

Neck is found by local vertical shifting of a rectangle (5×15 pixels) determined by the ellipse's semiminor axis to the region where the most uptake is detected since we are looking for the lower edge of the parietal bone which accumulates most radiopharmaceutical and is surrounded with soft tissue. Rectangle's orientation is preserved during the vertical shifting since the fitted ellipse is already detected at the right angle.

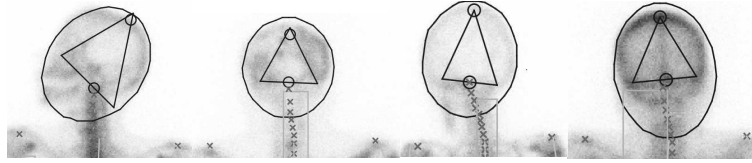


Figure 8: Examples of head detection in various orientations

3.3.5 Thoracic part (vertebrae, ribs).

Vertebrae have more or less specific intervertebral spaces [16], the only problem is that on a bone scintigram only a planar projection of the spine is visible. Since the spine is longitudinally curved, the vertebral spatial relations vary due to different axial orientation of the patients. Average intervertebral disc spaces have been experimentally determined from normal skeletons. After the approximate spine ROI is determined, it is divided into 10 vertical parts according to the predefined intervertebral disc sizes. These parts are then narrowed and shifted to the regions with the highest number of pre-detected peaks. This procedure is necessary in cases of patients with curved spine (scoliosis) in order to follow the spine form.

Ribs are the most difficult skeletal region to detect since they are quite unexpressive on bone scans, their formation can vary considerably and their contours can be disconnected in the case of stronger pathology. Using the detected vertebrae the ribs' ROI is defined between vertebra TH6 and TH11 as seen in Figure 9.

Many contour following techniques (i.e. 'turtle' procedure, crack following, border following ... [17]) exist in image processing but they all require a connected shape of the searched object. For rib contour detection we use morphology based image operations instead, particularly three well known algorithms (dynamic binarization, dilation / skeletonization [18] and Hough transform [19]).

The contour following algorithm for localizing the ribs uses short beam searches starting at the corresponding vertebrae and ending at the rib end. Length of the beam equals the width of the corresponding vertebra. The search is controlled with the anticipated rib curvature so it can skip the invisible rib parts, which can appear in scans of patients with stronger pathologies. This possibility makes the detection of the rib's end difficult (beam search can find a gap or the rib end). This is resolved by calculating the followed contour's length so the following can stop at the expected rib length if there is no more uptake in the contour direction present. There is a possibility of algorithm detecting a missing rib which is very rare and therefore this situation was not addressed.

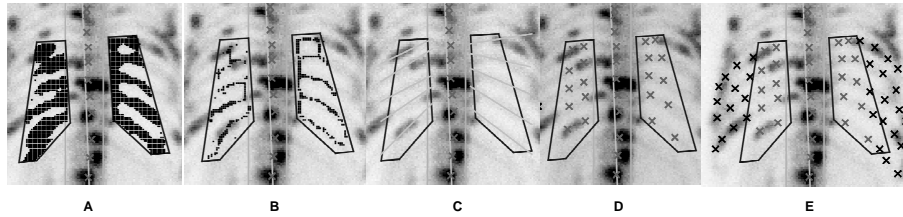


Figure 9: Rib detection steps example on a skeleton with strong pathology. (A) Rib ROI is binarized, (B) binarized image is skeletonized, (C) Hough transform of linear equation is calculated on skeleton points, (D) reference points are estimated using results of the Hough transform, (E) rib contours are individually followed by the contour following algorithm which uses background knowledge of anticipated rib shape.

3.3.6 Lower and upper extremities (femur, knee, tibia, fibula, feet, humerus, elbow, radius and ulna).

Extremities are often partly absent from whole-body scan because of the limited gamma camera detector width. In scans observed, a maximum of 61cm width is usually not enough to capture entire extremities. The regions of humerus, ulna and radius as well as femur, tibia and fibula bone are located with the use of controlled beam search. The beam lengths are estimated from skeletal relationships (i.e. femur length is estimated as 78% of the distance between the neck nape and the sacrum starting point). The detection is designed in such a way that a part or entire extremity or head may not be visible in the scan.

3.4 Diagnosing pathologies with machine learning

The obtained reference points can be used in two ways to segment a scan. One way is to segment scintigram only by extracting bones along the detected reference points with some pre-defined offset width. This type of segmentation was used in the classification part of our study. Since there is only a limited number of reference points we can extract only 26 bones or bone regions (i.e. extremities, lumbar, thoracic and cervical spine, 10 ribs, bones in pelvic region and the head). Some extracted bones are shown in Figure 10(a).

Another possibility of segmenting the scintigram is to map some standard predefined skeletal mask over the scan observed using the detected reference points as shown in Figure 10(c). The skeletal mask represented with polygons can be defined by a radiologist on some scan. The algorithm triangulates the scan using the detected reference points. A new scan is triangulated in the same way so the defined skeletal mask can be mapped. Mapping is carried out with linear transform for each triangle. The defined skeletal mask polygons are transformed with a linear operation which multiplies the polygon vertices

$p_{im}(x_{im}, y_{im})$ with the matrix A calculated from the belonging triangle coordinates in the original image $v_{1o}(x_{1o}, y_{1o}), v_{2o}(x_{2o}, y_{2o}), v_{3o}(x_{3o}, y_{3o})$ and in the new image $v_{1m}(x_{1m}, y_{1m}), v_{2m}(x_{2m}, y_{2m}), v_{3m}(x_{3m}, y_{3m})$.

$$A = \begin{bmatrix} x_{1m} & x_{2m} & x_{3m} \\ y_{1m} & y_{2m} & y_{3m} \\ 1 & 1 & 1 \end{bmatrix} \cdot \begin{bmatrix} x_{1o} & x_{2o} & x_{3o} \\ y_{1o} & y_{2o} & y_{3o} \\ 1 & 1 & 1 \end{bmatrix}^{-1}, p_{im} = A \cdot p_{io}$$

Obtained images of individual bones were parameterized using the ArTeX algorithm [20]. It uses association rules to describe images in a rotation and illumination-invariant manner. Rotation invariance is very important in this case since it compensates different patients' positions inside the camera, whereas the illumination compensates different absorption of radiopharmaceutical throughout the body.

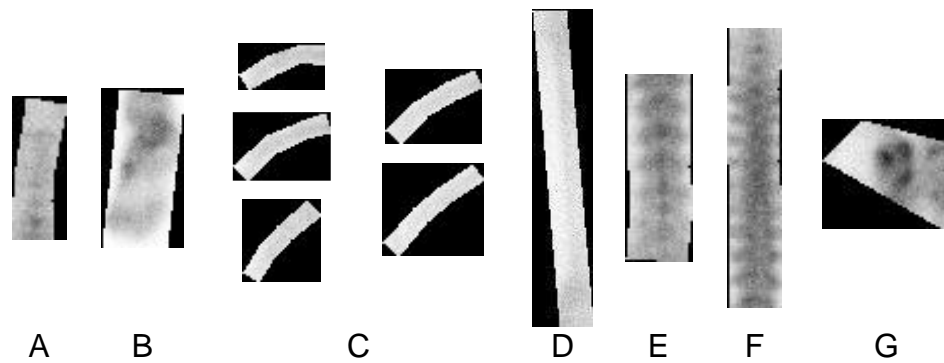
Bones were described with several hundreds of automatically generated attributes. They were used for training the SVM [21] learning algorithm implemented in Weka [22] (SMO algorithm). In our preliminary experiments pathologies were not discriminated, i.e. bones were labelled with only two possible diagnoses (no pathology, pathology). In 21% of scans no pathology or other artifacts were detected by expert physicians. In the remaining 79% of the scans at least one pathology or artifact was observed.

4 Results

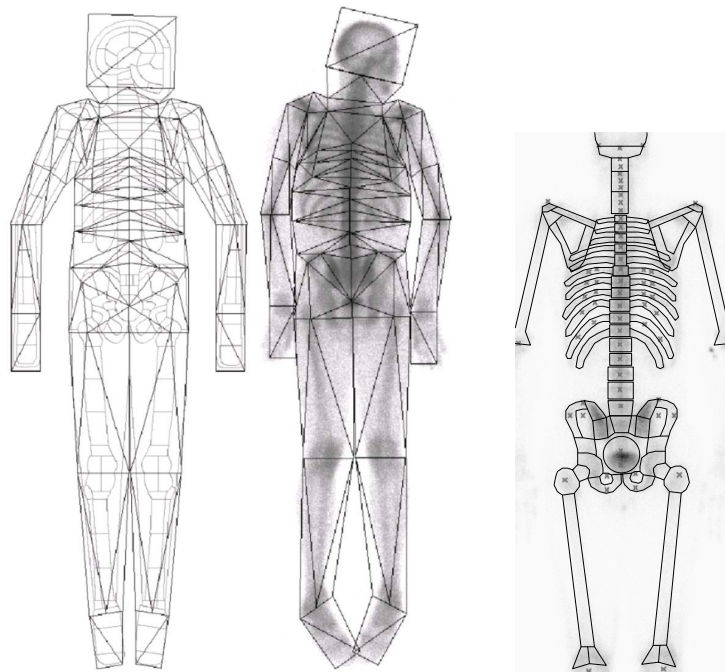
4.1 Segmentation

Approximately half of the scans were used for tuning the parameters required for reference point detection and another half to test the proposed algorithms. All 246 patients examined from October 2003 to March 2004 were used as the tuning set and 221 patients examined from April 2004 to June 2004 were used as the test set. In the tuning set there were various non-osseous uptakes in 38.9% of the images, 47.5% images with the visible injection point and 6.8% images of children/adolescents with the visible growth zones. Similar distribution was found in the test set (34.5% non-osseous uptakes, 41.0% visible injection points and 2.85% children/adolescents). Most of the artifacts were minor radioactivity points from urine contamination in pelvic region or other parts (81.4% of all artifacts) whereas only few other types were observed (urinary catheters 13%, artificial hips 4% and lead accessories 1.6%). We have observed that there were no miss-detected reference points in children/adolescents with the visible growth zones since all the bones are homogenous, have good visibility and are clearly divided with growth zones. The algorithm works for adult and children/adolescents patients without user intervention. Results of detecting reference points on the test set are shown in the Table 1.

Results are presented for different types of pathologies because we have expected that the degree of pathology affects the quality of detection process. The results showed that there are no major differences in the reference point



(a) Examples of extracted bones (A - cervical spine, B foot, C - ribs, D - femur, E - lumbar spine, F - thoracic spine, G - sacroiliac joint)



(b) Example of triangulated scans with standard skeletal mask

(c) Example of mapped standard skeletal mask with the detected reference points

Figure 10: Using reference points for scintigraphy segmentation

detection between different pathological groups.

The algorithm was implemented in a system called "Skeleton 1.2" [14] (written in Java 2 (SE) v 1.4.2) (Figure 11). The current system includes image editing, filtering with different linear filters, conversions to other formats, storing images in database with batch procedures, XML exports of reference points, manual correction of reference points, image annotation and region localization using the scalable correlation. We have also tested the accuracy of bone region localization using correlation with generalized bone region images which in addition to bigger time complexity gave worse results compared to the proposed algorithm. All high complexity algorithms were avoided and applied algorithms were optimized in the sense of computational complexity. The detection of reference points on both anterior and posterior image takes approximately 3s on Pentium 4, 2.8GHz, 1GB RAM.

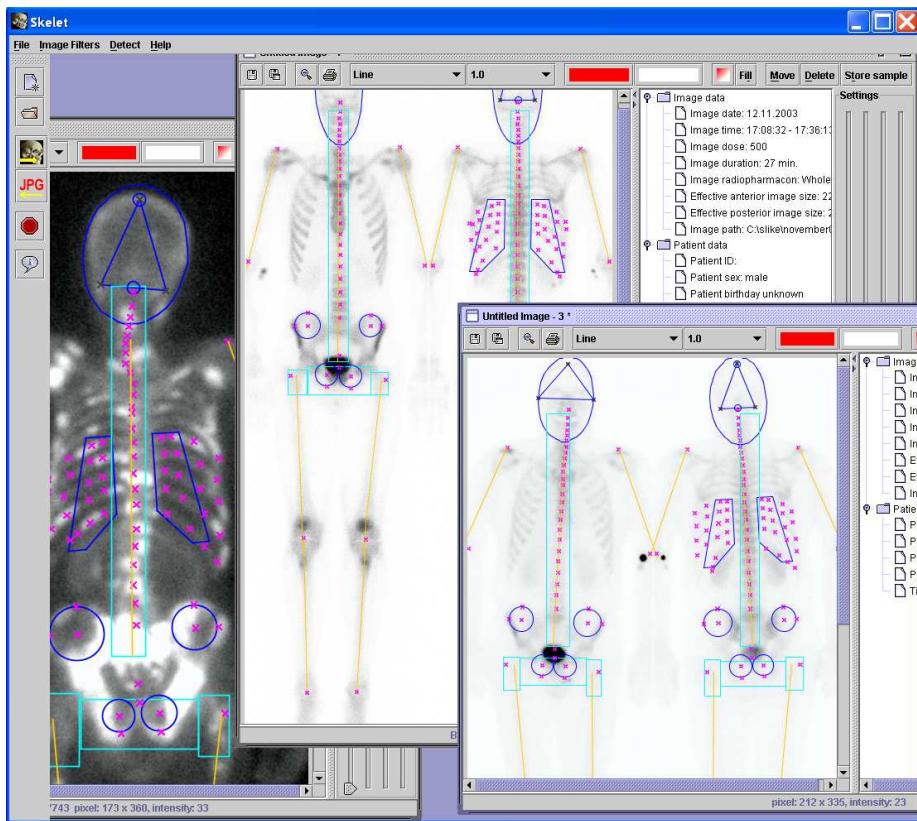


Figure 11: View of the program "Skeleton"

4.2 Machine learning results

From our complete set of 467 patients, pathologies were thoroughly evaluated by physicians for 268 patients. These 268 patients were used for evaluation of machine learning approach by using ten-fold cross validation. Results are shown in Table 2. They are quite satisfactory, given the high number of different bones (158 visible for an individual adult patient). The bones were grouped in ten relevant groups, for preliminary classification those groups were divided only in two (pathological and normal) classes. Ten groups were chosen because the poor technical quality of the images hinders more detailed scintigraphy segmentation and automatically segmented bone regions would be more often mislocated. Further work on recognition of different pathological conditions is in progress.

5 Discussion

The detection of the reference points gave excellent results for all bone regions except for the ribs and the extremities where some parts were missing in the scan. The extremities were mainly miss-detected in the cases where the humerus bone was partially missing.

As expected, the detection of ribs was the most difficult. The results show that in 14% to 20% of scans there were difficulties in detecting ribs. The ribs in thoracic part were hard to follow due to a vague expression. This usually means one rib is missed or not followed to the very end which we intend to improve in the future. In the present system (Figure 11) such reference points can be manually repositioned by the expert physician.

Since a robust segmentation algorithm should not fail on partial skeletal images, which is often the case in clinical routine (18% of the scans in our study), special attention has been paid to such cases (e.g. amputees and skeletal parts entirely invisible in the scan). In the results such cases do not stand out from the normal scans.

The automatically detected reference points can be used for mapping a standard skeletal reference mask, which to our belief, is the best way to find individual bones on scintigrams since individual bones are often not expressive enough to follow their contour. An example of such mask mapping and extracted bones is shown on Figure 10(c) and 10(a).

While our experimental results with machine learning are quite satisfactory, one must bear in mind that they were obtained for a simplified (two class) problem only. In our case simply extending a problem to a multi-class paradigm is not acceptable, since the bone may be assigned several different pathologies at the same time. In our new approach which we are currently developing, the problem will be rephrased to the multi-label learning problem where each bone will be labelled with a nonempty subset of all possible labels [23; 24].

6 Conclusion

The presented computer-aided system for bone scintigraphy is a step forward in automating routine medical procedures. Some standard image processing algorithms were tailored and used in combination to achieve the best reference point detection accuracy on scintigraphic images which have technically very low resolution. Because of poorer image resolution compared to radiography, the presence of artifacts and pathologies necessitate that algorithms use as much background knowledge on anatomy and spatial relations of bones as possible in order to work satisfactorily. This combination gives quite good results and we expect that further studies on automatic scintigrams diagnosing using reference points for image segmentation will give more accurate and reliable results than previous studies, negligent to the segmentation.

This approach opens a new view on automatic bone scintigraphy evaluation, since in addition to detection of point-like high-uptake lesions there are also:

- more accurate and reliable evaluation of bone symmetry when looking for skeletal abnormalities. Many abnormalities can be spotted only when the symmetry is observed (differences in length, girth, curvature etc.),
- detection of lesions with low-uptake or lower activity due to metallic implants (i.e. artificial heap),
- possibility of comparing uptake ratios among different bones,
- more complex pathology detection with combining pathologies of more bones (i.e. arthritis in joints)
- possibility of automatic reporting of bone pathologies in written language for educational purposes.

The machine learning approach described in this work is in an early stage of development. However, the preliminary results are encouraging and the multilabel learning framework will make them more useful for clinical routine work.

Acknowledgement

This work was supported by the Slovenian Ministry of Higher Education, Science and Technology through the research programme P2-0209. Special thanks to nuclear medicine specialist Jure Fettich and the chief technologist Ivan Slodnjak at the University Medical Centre in Ljubljana for their help.

Table 1: Number of correctly detected reference points on the test set in different degrees of pathologies. Both frequencies and percentages are given.

<i>Bone</i>	<i>no pathology</i>		<i>slight pathology</i>		<i>strong pathology</i>		<i>super-scan</i>		<i>all</i>	
<i>females</i>	<i>22</i>		<i>78</i>		<i>15</i>		<i>1</i>		<i>116</i>	
ilium	22	100%	76	97%	13	87%	0	0%	111	96%
pubis	22	100%	76	97%	14	93%	1	100%	113	97%
trochanter	22	100%	77	99%	15	100%	1	100%	115	99%
shoulder	22	100%	78	100%	14	93%	1	100%	115	99%
extremities	21	96%	74	95%	15	100%	1	100%	111	96%
spine	22	100%	78	100%	14	93%	1	100%	115	99%
ribs	16	73%	70	90%	12	80%	1	100%	99	85%
neck	22	100%	76	97%	15	100%	1	100%	114	98%
<i>average</i>	<i>96%</i>		<i>97%</i>		<i>93%</i>		<i>88%</i>		<i>96%</i>	
<i>males</i>	<i>24</i>		<i>55</i>		<i>24</i>		<i>2</i>		<i>105</i>	
ilium	24	100%	55	100%	20	83%	2	100%	101	96%
pubis	22	92%	54	98%	23	96%	2	100%	101	96%
trochanter	24	100%	55	100%	24	100%	2	100%	105	100%
shoulder	24	100%	55	100%	24	100%	2	100%	105	100%
extremities	20	83%	48	87%	24	100%	2	100%	94	90%
spine	24	100%	53	96%	24	100%	2	100%	103	98%
ribs	19	79%	46	84%	24	100%	2	100%	91	87%
neck	22	92%	53	96%	24	100%	2	100%	101	96%
<i>average</i>	<i>93%</i>		<i>95%</i>		<i>97%</i>		<i>100%</i>		<i>95%</i>	
<i>sum</i>	<i>46</i>		<i>133</i>		<i>39</i>		<i>3</i>		<i>221</i>	
ilium	46	100%	131	98%	33	85%	2	67%	212	96%
pubis	44	96%	130	98%	37	95%	3	100%	214	97%
trochanter	46	100%	132	99%	39	100%	3	100%	220	100%
shoulder	46	100%	133	100%	38	97%	3	100%	220	100%
extremities	41	89%	122	92%	39	100%	3	100%	205	93%
spine	46	100%	131	98%	38	97%	3	100%	218	99%
ribs	35	76%	116	87%	36	92%	3	100%	190	86%
neck	44	96%	129	97%	39	100%	3	100%	215	97%
<i>average</i>	<i>95%</i>		<i>94%</i>		<i>96%</i>		<i>96%</i>		<i>96%</i>	

Table 2: First results with machine learning on two-class problem (normal, pathology).

Bone group	Classification accuracy %	spec.%	sensit.%
Cervical spine	75,9	80,0	77,8
Feet	83,8	84,1	68,0
Skull posterior	94,7	88,2	100,0
Ilium bone	87,3	87,6	82,8
Lumbal spine	71,4	75,7	65,4
Femur and tibia	88,9	84,6	73,3
Pelvic region	92,2	90,7	85,0
Ribs	98,1	92,5	91,7
Scapula	91,4	90,9	90,9
Thoracic spine	82,0	79,2	61,5
Average	86,6	85,4	79,6

References

- [1] Müller V., Steinhagen J., de Wit M., and Bohuslavizki H. K. Bone Scintigraphy in Clinical Routine. *Radiol Oncol*, 35(1):21–30, 2001.
- [2] Hendler A. and Hershkop M. When to Use Bone Scintigraphy. It Can Reveal Things Other Studies Cannot. *Postgraduate Medicine*, 104(5):54–66, 11 1998.
- [3] Noguchi M., Kikuchi H., Ishibashi M., and Noda S. Percentage of the Positive Area of Bone Metastasis is an Independent Predictor of Disease Death in Advanced Prostate Cancer. *British Journal of Cancer*, (88):195–201, 2003.
- [4] Bernauer J. Zur Semantischen Rekonstruktion Medizinischer Begriffssysteme. Habilitationsschrift, Institut für Medizinische Informatik, Univ. Hildesheim, 1995.
- [5] Berning K.-C. *Zur Automatischen Befundung und Interpretation von Ganzkörper-Skelettszintigrammen*. PhD thesis, Institut für Medizinische Informatik, Universität Hildesheim, 1996.
- [6] Benneke A. Konzeption und Realisierung Eines Semi-Automatischen Befundungssystems in Java und Anbindung an ein Formalisiertes Begriffssystem am Beispiel der Skelett-Szintigraphie. Diplom arbeit, Institut für Medizinische Informatik, Universität Hildesheim, mentor Prof. Dr. D.P. Pretschner, 1997.
- [7] Maisey M.N., Natarajan T.K., Hurley P.J., and Wagner H.N. Jr. Validation of a Rapid Computerized Method of Measuring ^{99m}Tc Pertechnetate Uptake for Routine Assessment of Thyroid Structure and Function. *J Clin Endocrinol Metab*, 36:317–322, 1973.
- [8] Yin T.K. and Chiu N.T. A Computer-Aided Diagnosis for Locating Abnormalities in Bone Scintigraphy by a Fuzzy System With a Three-Step Minimization Approach. *IEEE Transactions on Medical Imaging*, 23(5):639–654, 5 2004.
- [9] Kukar M., Kononenko I., Grošelj C., Kralj K., and Fettich J. Analysing and Improving the Diagnosis of Ischaemic Heart Disease with Machine Learning. *Artificial Intelligence in Medicine*, 16:25–50, 1999.
- [10] David G. Lowe. Distinctive image features from scale-invariant keypoints. *Int. J. Comput. Vision*, 60(2):91–110, 2004.
- [11] H. Murase and S. Nayar. Visual learning and recognition of 3-d objects from appearance. *IJCV*, 14(1):5–24, 1 1995.

- [12] Jammal G. and Bijaoui A. DeQuant: a Flexible Multiresolution Restoration Framework. *Signal Processing*, 84(7):1049–1069, 7 2004.
- [13] Weiner M. G., Jenicke L., Mller V., and Bohuslavizki H. K. Artifacts and Non-Osseous Uptake in Bone Scintigraphy. Imaging Reports of 20 Cases. *Radiol Oncol*, 35(3):185–91, 2001.
- [14] Šajin Luka. Program source code, 2006. lkm.fri.uni-lj.si/skelet/skelet.zip.
- [15] Eberly D. Information about ellipses. Magic Software, Inc., 12 2003.
- [16] Holmaas G., Frederiksen D., Ulvik A., Vingsnes S. O., Ostgaard G., and H. Nordli. Identification of thoracic intervertebral spaces by means of surface anatomy: a magnetic resonance imaging study. *Acta Anaesthesiologica Scandinavica*, 50(3):368–373(6), 2006.
- [17] Kindratenko V. *Development and Application of Image Analysis Techniques for Identification and Classification of Microscopic Particles*. PhD thesis, Universitaire Instelling Antwerpen, Departement Scheikunde, 1997.
- [18] Blum H. *Models for the Perception of Speech and Visual Form*. MIT Press, 1967.
- [19] Hough P.V.C. Machine analysis of bubble chamber pictures. International Conference on High Energy Accelerators and Instrumentation, CERN, 1959.
- [20] Bevk M. and Kononenko I. Towards Symbolic Mining of Images with Association Rules: Preliminary Results on Textures. In Brito P. and Noirhomme-Fraiture M., editors, *ECML/PKDD 2004: proc. of the workshop W2 on symbolic and spatial data analysis: mining complex data structures*, pages 43–53, 2004.
- [21] Cristianini N. and Shawe-Taylor J. *An Introduction to Support Vector Machines and Other Kernel-Based Learning Methods*. Cambridge University Press, 2000.
- [22] I.H. Witten and E. Frank. *Data Mining: Practical Machine Learning Tools and Techniques with Java Implementations*. Morgan Kaufmann, 1999.
- [23] Shen X., Boutell M., Luo J., and Brown C. Multi-Label Machine Learning and its Application to Semantic Scene Classification. In *Proceedings of the 2004 International Symposium on Electronic Imaging (EI 2004)*, San Jose, California, 2004.
- [24] McCallum A. Multi-Label Text Classification with a Mixture Model Trained by EM. In *Proc. AAAI'99 Workshop on Text Learning*, 1999.